18 *Chem. Mater.* **2010,** *22,* 18–26
DOI:10.1021/cm901684m

CHEMISTRY OF MATERIALS
Article

Free-Standing Mesoporous Silica/Carbon Composite Films with Crystalline Silica Wall from Ethylene-Bridged Organosilane

Sung Soo Park,[†] Yuin Jung,[†] Chunfeng Xue,[‡] Renchao Che,[‡] Dongyuan Zhao,[‡] and Chang-Sik Ha*,[†]

[†]*Department of Polymer Science and Engineering, Pusan National University, Geumjeong-gu, Busan 609-735, Korea, and* [‡]*Department of Chemistry, Advanced Materials Laboratory, Fudan University, Shanghai 200433, P. R. China*

Received June 17, 2009. Revised Manuscript Received October 20, 2009

Free-standing periodic mesoporous organosilica (PMO) films were grown at the interface of an ethylene-bridged organosilica and surfactant template via a self-assembly process. After the pyrolysis of the PMO films with ethylene-bridged organosilica moieties in the pore walls under an Ar flow at temperatures ranging from 400 to 900 °C, free-standing mesoporous silica/carbon composite films were obtained. The composite films had a highly ordered periodic mesostructure with a hexagonal closed-packed arrangement of channels running parallel to the surface. The mesopore walls of the films pyrolyzed above 700 °C in the presence of alkali metal ions had a cristobalite structure at the pore walls. When the pyrolysis temperature was between 400 and 900 °C, the pore diameter, surface area, and pore volume of the silica/carbon composite films were 18.2−30.5 Å, 172−690 $m^2\ g^{-1}$, and 0.18−0.64 $cm^3\ g^{-1}$, respectively.

Introduction

Mesoporous materials are of considerable interest for many applications, and a range of synthesis strategies have been developed for the preparation of well-ordered mesoporous materials.[1−5] It is now possible to prepare mesoporous materials based on pure silica, heteroatom doped silica, organosilica, nonsiliceous metal oxide, metal, and carbon frameworks.[1−4,6−10] Mesoporous silica is the one most commonly used as a starting material or hard template for nanocasting to obtain mesoporous carbon and other nonsiliceous mesoporous materials.[3,4,8−10] Nanoporous silica can also be used to fabricate silica-based composite materials, such as metal/silica or metal oxide/silica,[11−13] polymer/silica,[14,15] carbon/silica composites, etc.[5,16−20] Silica-based composites are interesting because of their attractive optical,[12,21]

*Corresponding author. Fax: +82 51 514 4331. Tel: +82 51 510 2407. E-mail: csha@pusan.ac.kr.

(1) (a) Kresge, C. T.; Leonowicz, M. E.; Roth, W. J.; Vartuli, J. C.; Beck, J. S. *Nature* **1992**, *359*, 710–712. (b) Beck, J. S.; Vartuli, J. C.; Roth, W. J.; Leonowicz, M. E.; Kresge, C. T.; Schmitt, K. D.; Chu, C. T.-W.; Olson, D. H.; Sheppard, E. W.; McCullen, S. B.; Higgins, J. B.; Schlenker, J. L. *J. Am. Chem. Soc.* **1992**, *114*, 10834–10843.
(2) (a) Corma, A. *Chem. Rev.* **1997**, *97*, 2373–2419. (b) Ying, J. Y.; Mehnert, C. P.; Wong, M. S. *Angew. Chem., Int. Ed.* **1999**, *38*, 56–77.
(3) (a) Linden, M.; Schacht, S.; Schuth, F.; Steel, A.; Unger, K. K. *J. Porous Mater.* **1998**, *5*, 177–193. (b) Stein, A. *Adv. Mater.* **2003**, *15*, 763–775.
(4) (a) Ciesla, U.; Schuth, F. *Microporous Mesoporous Mater.* **1999**, *27*, 131–149. (b) Tagushi, A.; Schuth, F. *Microporous Mesoporous Mater.* **2005**, *77*, 1–45. (c) Schuth, F. *Chem. Mater.* **2001**, *13*, 3184–3195. (d) Schuth, F.; Schmidt, W. *Adv. Mater.* **2002**, *14*, 629–638.
(5) Yang, Z.; Xia, Y.; Mokaya, R. *J. Mater. Chem.* **2006**, *16*, 3417–3425.
(6) (a) On, D. T.; Desplantier-Giscard, D.; Danumah, C.; Kaliaguine, S. *Appl. Catal. A: Gen.* **2002**, *222*, 299–357. (b) Qye, G.; Sjöblom, J.; Stöcker, M. *Adv. Colloid Interface Sci.* **2001**, *89*, 439–466.
(7) (a) Stein, A.; Melde, B. J.; Schroden, R. C. *Adv. Mater.* **2000**, *12*, 1403–1419. (b) Sayari, A.; Hamoudi, S. *Chem. Mater.* **2001**, *13*, 3151–3168. (c) Scott, B. J.; Wirnsberger, G.; Stucky, G. D. *Chem. Mater.* **2001**, *13*, 3140–3150. (d) Sanchez, C. L. B.; Chaput, F.; Boilot, J. P. *Adv. Mater.* **2003**, *15*, 1969–1994. (e) Hatton, B.; Landskron, K.; Whitnall, W.; Perovic, D.; Ozin, G. A. *Acc. Chem. Res.* **2005**, *38*, 305–312. (f) Hoffmann, F.; Cornelius, M.; Morell, J.; Fröba, M. *Angew. Chem., Int. Ed.* **2006**, *45*, 3216–3251.
(8) (a) Li, W. C.; Lu, A. H.; Weidenthaler, C.; Schuth, F. *Chem. Mater.* **2004**, *16*, 5676–5681. (b) Xia, Y.; Mokaya, R. *J. Mater. Chem.* **2005**, *15*, 3126–3131. (c) Armatas, G. S.; Kanatzidis, M. G. *Nature* **2006**, *441*, 1122–1125.
(9) Ryoo, R.; Joo, S. H.; Kruk, M.; Jaroniec, M. *Adv. Mater.* **2001**, *13*, 677–681.
(10) (a) Lee, J.; Han, S.; Hyeon *J. Mater. Chem.* **2004**, *14*, 478–486. (b) Yang, H. F.; Zhao, D. Y. *J. Mater. Chem.* **2005**, *15*, 1217–1231.
(11) Schubert, U. *Adv. Eng. Mater.* **2004**, *6*, 173–176.
(12) Teyssier, J.; Le Dantec, R.; Galez, C.; Mugnier, Y.; Bouillot, J.; Plenet, J.-C. *J. Non-Cryst. Solids* **2004**, *341*, 152–156.
(13) Chastellain, M.; Petri, A.; Gupta, A.; Rao, K. V.; Hofmann, H. *Adv. Eng. Mater.* **2004**, *6*, 235–241.
(14) Azioune, A.; Slimane, A. B.; Hamou, L. A.; Pleuvy, A.; Chehimi, M. M.; Perruchot, C.; Armes, S. P. *Langmuir* **2004**, *20*, 3350–3356.
(15) Garcia, M.; van Vliet, G.; Jain, S.; Schrauwen, B. A. G.; Sarkissov, A.; van Zyl, W. E.; Boukamp, B. *Rev. Adv. Mater. Sci.* **2004**, *6*, 169–175.
(16) Moreno-Castilla, C.; Maldonado-Hodar, F. J. *Phys. Chem. Chem. Phys.* **2000**, *2*, 4818–4822.
(17) Scian, A. N.; Volzone, C. *Bol. Soc. Esp. Ceram. Vidrio* **2001**, *40*, 279–284.
(18) Alvaro, M.; Atienzar, P.; Bourdelande, J. L.; Garcia, H. *Chem. Commun.* **2002**, 3004–3005.
(19) Giunta, P. R.; van de Burgt, L. J.; Stiegman, A. E. *Chem. Mater.* **2005**, *17*, 1234–1240.
(20) (a) Pang, J.; John, V. T.; Loy, D. A.; Yang, Z.; Lu, Y. *Adv. Mater.* **2005**, *17*, 704–707. (b) Toury, B.; Babonneau, F. *J. Eur. Ceram. Soc.* **2005**, *25*, 265–270. (c) Masse, S.; Laurent, G.; Babonneau, F. *J. Non-Cryst. Solids* **2007**, *353*, 1109–1119. (d) Toury, B.; Blum, R.; Goletto, V.; Babonneau, F. *J. Sol−Gel Sci. Technol.* **2005**, *33*, 99–102. (e) Coutinho, D.; Gorman, B.; Ferraris, J. P.; Yang, D. J.; Balkus, K. J. *Microporous Mesoporous Mater.* **2006**, *91*, 276–286.
(21) Chang, H.; Okuyama, K.; Szymanski, W. W. *Aerosol Sci. Technol.* **2003**, *37*, 735–751.

 Published on Web 12/08/2009 © 2009 American Chemical Society

magnetic,[13] thermal,[22,23] mechanical,[22] and electrical[24] properties. Silica/carbon composites are particularly versatile materials for many potential applications in electrochemical devices[24] and selective solar absorber materials.[25] Silica/carbon composites can be prepared using a variety of methods including the sol-gel process followed by carbonization,[16,26] pyrolysis of a suitable carbon precursor (e.g., polyacrylonitrile) in a porous silica matrix,[19] or carbonization of organosilica/surfactant mesophases.[20]

Periodic mesoporous materials with various compositions and controllable morphologies have attracted considerable attention on account of their versatility in separation, catalysis, nanoreactors, and sensors.[2b,27] Fabrication of the desired morphologies as well as control of the composition, structure, porosity, etc., are important for a variety of practical applications. Three research groups[28−30] have reported the formation of ordered mesoporous silica films at the air-water interface. Recently, we described the surfactant-template synthesis of high-quality free-standing and oriented PMO films grown at the air-water interface.[31]

SiO_2 materials can show enhanced chemical and thermal stability with respect to their amorphous counterparts.[32] Catalysts used for the crystallization of silica glass include carbon,[33] water,[34] noble metals,[35] and alkali ions.[36] Venezia et al.[37] reported the effect of alkali ions on the amorphous to crystalline phase transition of silica powders. Zhao et al.[32] reported the crystallization of amorphous SiO_2 microtubes catalyzed by lithium. Shinohara et al.[38] carried out quantitative analysis of tridymite and cristobalite that had been crystallized in rice husk ash by heating. Different silica minerals are formed depending on the temperature and pressure during crystallization. Under high pressures (~25 GPa) at room temperature, Huang et al.[39] reported a cristobalite to stishovite transformation. Tsuchida and Yagi[40] reported a phase transformation from cristobalite and quartz to stishovite and another phase at high pressure (~60 GPa). However, the crystalline silica materials prepared by previous researchers did not have ordered mesostructures or free-standing film morphology.

In this study, free-standing mesoporous silica/carbon composite films were synthesized from an ethylene-bridged organosilica/surfactant mesophase via a pyrolysis process. The composite films had a highly ordered periodic mesostructure with a hexagonal closed-packed arrangement of channels running parallel to the surface of the film. The mesopore walls of the films pyrolyzed above 700 °C in the presence of alkali metal ions were composed of crystalline silica with a cristobalite structure and had uniform pore diameter, high surface area, and large pore volume.

Experimental Section

Chemicals. Octadecyltrimethylammonium bromide (C_{18}TMABr, Aldrich) and 1,2-bis(triethoxysilyl)ethane (BTEE, 96%, Aldrich) were used as a structure-directing agent and organosilica source, respectively. Sodium hydroxide (95%, Katayama chemical), absolute ethanol (99.9% (v/v), Hayman), and a HCl solution (37 wt % in water, Aldrich) were used as purchased.

Synthesis of Free-Standing Mesoporous Silica/Carbon Composite Film with Crystalline Silica Wall. Oriented periodic mesoporous organosilica (PMO) films at the air-water interface were synthesized using the following reactant mole ratios and the procedure reported by Park et al.:[31] 1.0:0.57:2.36:353 BTEE:C_{18}TMABr:NaOH:H_2O, where C_{18}TMABr is the cationic surfactant $CH_3(CH_2)_{17}N(CH_3)_3Br$ and BTEE is the organosilica source reagent $(C_2H_5O)_3SiCH_2CH_2Si(OC_2H_5)_3$. The surfactant solution was mixed with BTEE, stirred at 40 °C for 12 h, and heated in a polypropylene bottle. The film-forming process works well under static conditions at 95 °C over a reaction time of 8 h. The as-synthesized free-standing PMO film was rinsed with EtOH-H_2O (volume ratio of 1:1, v/v) solution. Energy-dispersive X-ray (EDX) spectroscopy revealed a Si/Na ratio of 9.5 in the as-synthesized PMO film. Finally, the as-synthesized PMO film was pyrolyzed from 400 to 900 °C for 3 h in an Ar flow. Most of the organic moieties in the framework are degraded between about 300 and 600 °C (see Figure S1 in the Supporting Information). Above 600 °C, however, there is no further severe degradation of organic moieties, as shown in Figure S1 of the Supporting Information. Taking these into consideration, therefore, we carried out pyrolysis with a heating rate of 1 °C/min below 600 °C to effectively control the degradation, but with 5 °C/min above 600 °C as under normal conditions generally used to prepare mesoporous carbon materials. The pyrolyzed films were labeled as PMO film *X*, where *X* represents the pyrolysis temperature. Surfactant-extraction of the as-synthesized PMO films was carried out using the following process: the as-synthesized film (0.1 g)

(22) Biercuk, M. J.; Llaguno, M. C.; Radosavljevic, M.; Hyun, J. K.; Johnson, A. T.; Fischer, J. E. *Appl. Phys. Lett.* **2002**, *80*, 2767–2769.
(23) Gong, Q.-M.; Li, Z.; Li, D.; Bai, X.-D.; Liang, J. *Solid State Commun.* **2004**, *131*, 399–404.
(24) Gavalas, V. G.; Andrews, R.; Bhattacharyya, D.; Bachas, L. G. *Nano Lett.* **2001**, *1*, 719–721.
(25) Mastai, Y.; Polarz, S.; Antonietti, M. *Adv. Funct. Mater.* **2002**, *12*, 197–202.
(26) Aguado-Serrano, J.; Rojas-Cervantes, M. L.; Lopez-Peinado, A. J.; Gomez-Serrano, V. *Microporous Mesoporous Mater.* **2004**, *74*, 111–119.
(27) Davis, M. E. *Nature* **2002**, *417*, 813–821.
(28) Yang, H.; Coombs, N.; Sokolov, I.; Ozin, G. A. *Nature* **1996**, *381*, 589–592.
(29) Ruggles, J. L.; Holt, S. A.; Reynolds, P. A.; Brown, A. S.; Creagh, D. C.; White, J. W. *Phys. Chem. Chem. Phys.* **1999**, *1*, 323–328.
(30) Tolbert, S. H.; Schäffer, T. E.; Feng, J.; Hansma, P. K.; Stucky, G. D. *Chem. Mater.* **1997**, *9*, 1962–1967.
(31) (a) Park, S. S.; Ha, C.-S. *Chem. Commun.* **2004**, 1986–1987. (b) Park, S. S.; Ha, C.-S. *Chem. Mater.* **2005**, *17*, 3519–3523.
(32) Zhao, L.; Li, N.; Langner, A.; Steinhart, M.; Tan, T. Y.; Pippel, E.; Hofmeister, H.; Tu, K.-N.; Gösele, U. *Adv. Funct. Mater.* **2007**, *17*, 1952–1957.
(33) Deepak, F. L.; Gundiah, G.; Seikh, M. M.; Govindaraj, A.; Rao, C. N. R. *J. Mater. Res.* **2004**, *19*, 2216–2221.
(34) Wagstaff, F. E.; Richards, K. J. *J. Am. Ceram. Soc.* **1966**, *49*, 118–121.
(35) (a) Pol, V. G.; Gedanken, A.; Calderon-Moreno, J. *Chem. Mater.* **2003**, *15*, 1111–1118. (b) Garnica-Romo, M. G.; Gonzalez-Hernandez, J.; Hernandez-Landaverde, M. A.; Vorobiev, Y. V.; Ruiz, F.; Martinez, J. R. *J. Mater. Res.* **2001**, *16*, 2007–2012.
(36) (a) Jean, J. H.; Gupta, T. K. *J. Mater. Res.* **1992**, *7*, 3103–3112. (b) Palermo, A.; Vazquez, J. P. H.; Lee, A. F.; Tikhov, M. S.; Lambert, R. M. *J. Catal.* **1998**, *177*, 259–266.
(37) Venezia, A. M.; La Parola, V.; Longo, A.; Martorana, A. *J. Solid State Chem.* **2001**, *161*, 373–378.
(38) Shinohara, Y.; Kohyama, N. *Ind. Health* **2004**, *42*, 277–285.
(39) Huang, L.; Durandurdu, M.; Kieffer, J. *Nat. Mater.* **2006**, *5*, 977–981.
(40) Tsuchida, Y.; Yagi, T. *Nature* **1990**, *347*, 267–269.

was stirred in EtOH (15 mL) containing 37 wt % HCl (0.3 mL) at 60 °C for 12 h. The solids were filtered, washed, and dried at 100 °C for 12 h. The PMO film was labeled as PMO film-EX.

Characterization. Powder X-ray diffraction (XRD) patterns were obtained using a Rigaku Miniflex diffractometer (40 kV, 30 mA) with Cu K_α radiation at a wavelength of 1.541 Å. The adsorption/desorption isotherms of nitrogen at −196 °C were measured using a Nova 4000e surface area and pore size analyzer. All samples were outgassed at 180 °C for 12 h under vacuum ($p < 5 \times 10^{-6}$ Torr) in the degassing port of the adsorption analyzer. The pore size distribution curve was obtained from an analysis of the adsorption branch using the Barrett−Joyner−Halenda (BJH) method. Both as-synthesized and carbonized (at 900 °C) films (as shown in Figure S2 in the Supporting Information) were cut into small pieces on the order of ca. < 5 mm so that the film samples could be safely put into the sample holder. Scanning electron microscopy (SEM) images with energy-dispersive X-ray (EDX) analysis were obtained using a KEVEX Sigma microscope with an acceleration voltage of 20 kV. Prior to imaging, the samples were coated with gold using a HITACHI E-1010 sputter coater. Transmission electron microscopy (TEM) images were obtained using a JEOL 2021F microscope operating at 200 kV. The samples with KBr pellets were characterized by FT-IR spectroscopy at ambient atmosphere. All the spectra were recorded after averaging 24 scans at a 16 mm^{-1} resolution using a Shimadzu IR Prestige-21 spm with a Ge-KBr beam splitter. The ^{29}Si and ^{13}C cross-polarization (CP) MAS NMR spectra were obtained on a Bruker DSX400 spectrometer at room temperature with a 4 mm zirconia rotor spinning at 6 kHz (the resonance frequencies of ^{29}Si and ^{13}C CP MAS NMR were 79.5 and 100.6 MHz, respectively; a 90° pulse width of 5 μs, a contact time of 2 ms; and a recycle delay of 3 s for both ^{29}Si and ^{13}C CP MAS NMR (Korea Basic Science Institute Daegu Center, Korea)).

Results and Discussion

The as-synthesized free-standing PMO film was obtained with diameter of ca. 4 cm (see Figure S2 in the Supporting Information). After pyrolysis at 900 °C, the size of the film decreased to *ca.* 3 cm, suggesting a shrinkage of about 25%, which is similar to that for structural reduction (see Figure S2 in the Supporting Information). When the pyrolysis temperature was increased to 900 °C, the thickness of the composite film was reduced from 448 to 192 nm (Figure 1) due to the removal of the surfactant template from the channels with the concomitant condensation of the silanol groups in the pore walls.[28,31,41,42] This thickness reduction is also related to the decomposition of organic groups in the mesoporous ethylene-bridged organosilane framework.

TEM images of the as-synthesized PMO film formed at the air-water interface showed that the film has a highly ordered periodic mesostructure with a hexagonal

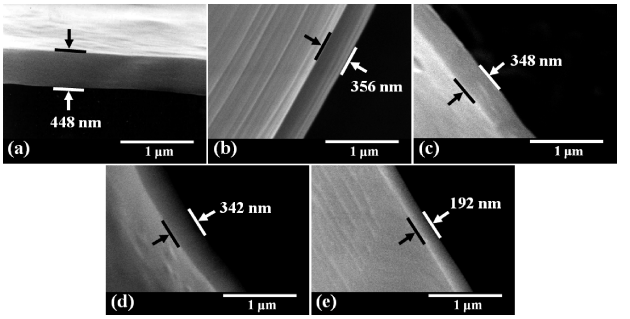

Figure 1. SEM images of the (a) Na ion-containing, as-synthesized PMO film and PMO films pyrolyzed (b) at 400, (c) 550, (d) 700, and (e) 900 °C, respectively.

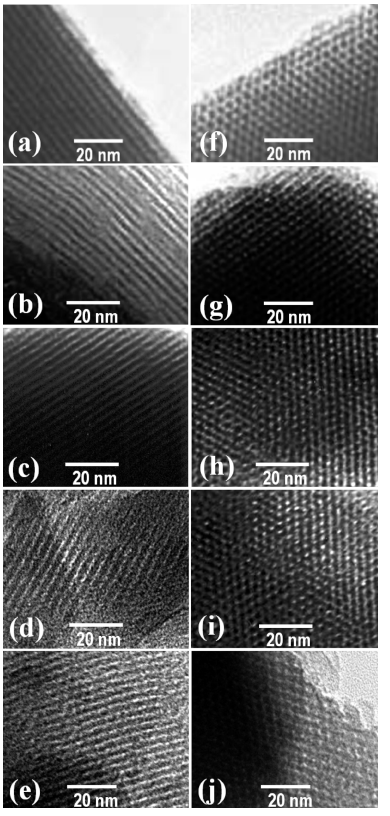

Figure 2. TEM images of (a, f) the Na ion-containing, as-synthesized PMO film and PMO films pyrolyzed at (b, g) 400, (c, h) 550, (d, i) 700, and (e, j) 900 °C, respectively, showing (a−e) a highly ordered periodic structure consistent with a hexagonal close-packed arrangement of channels running parallel to the surface of the films and (f−j) a hexagonal basal plane with a well-ordered hexagonal array.

closed-packed arrangement of channels running parallel to the film surface (Figure 2a).[31] The hexagonal periodicity of one-dimensional (1D) mesochannels viewed orthogonally to the film surface was observed at the bent edge of the film, as shown in Figure 2f.[31] After pyrolysis from 400 to 900 °C in an Ar flow, the ordered mesostructure of the films was retained with a 2D hexagonal symmetry, as shown in Figure 2b−e and g−j. Interestingly, with a pyrolysis temperature above 700 °C, crystalline silica was produced within the composite films as shown in the high-resolution TEM (HRTEM) image (Figure 3). The HRTEM image shows that the crystalline silica films have a cristobalite structure with an interlayer

(41) (a) Dag, Ö.; Yoshina-Ishii, C.; Asefa, T.; MacLachlan, M. J.; Grondey, H.; Coombs, N.; Ozin, G. A. *Adv. Funct. Mater.* **2001**, *11*, 213–217.
(42) Park, S. S.; An, B.; Ha, C.-S. *Microporous Mesoporous Mater.* **2008**, *111*, 367–378.

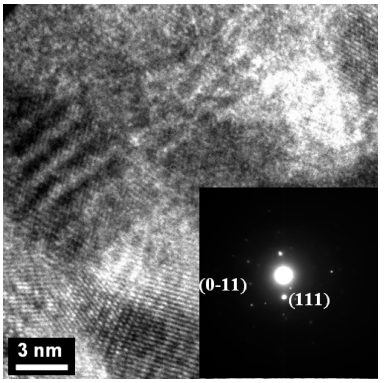

Figure 3. High-resolution TEM image of the PMO film pyrolyzed at 900 °C in an Ar flow. Inset shows a typical selected area electron diffraction pattern.

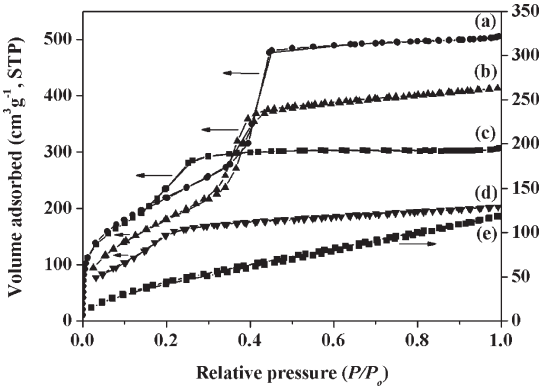

Figure 4. Nitrogen adsorption/desorption isotherms of (a) the Na ion-containing, as-synthesized PMO film and PMO films pyrolyzed at (b) 400, (c) 550, (d) 700, and (e) 900 °C, respectively.

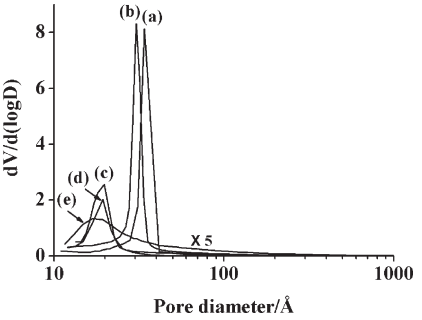

Figure 5. Pore size distributions obtained using the adsorption branch from the BJH method: (a) the Na ion-containing, as-synthesized PMO film and PMO films pyrolyzed at (b) 400, (c) 550, (d) 700, and (e) 900 °C, respectively.

spacing of 4 Å,[43] while the partial hexagonal periodicity of the 1D mesochannels is observed in some domains. This result is supported by the electron diffraction (ED) pattern in the inset of Figure 3.[43] N_2 sorption isotherms showed that the pore diameter, total pore volume, and total surface area of the surfactant-extracted PMO film (e.g., PMO film-EX) were 34.2 Å, 0.78 cm^3 g^{-1}, and 811 m^2 g^{-1}, respectively, as shown in Figures 4 and 5 and Table 1.

The pore diameter, total pore volume, and total surface area of the pyrolyzed film were determined from N_2 sorption isotherms to be 18.2−30.5 Å, 0.18− 0.64 cm^3 g^{-1}, and 172−690 m^2 g^{-1}, respectively. (Table 1, Figures 4 and 5) After pyrolysis at 700 °C, the surface area and pore volume due to the micropores increased to 479 m^2 g^{-1} and 0.20 cm^3 g^{-1}, respectively, while the total surface area and total pore volume decreased to 570 m^2 g^{-1} and 0.31 cm^3 g^{-1} ($S_{\text{Micropore}}/S_{\text{Total}}$ = 0.8 and $V_{\text{Micropore}}/V_{\text{Total}}$ = 0.7), respectively. This may be due to the shrinkage of the mesopore walls and the decomposition of the organic moiety in the framework. After pyrolysis at 900 °C, the surface area and pore volume of the micropores further decreased to 68.1 m^2 g^{-1} and 0.03 cm^3 g^{-1} ($S_{\text{Micropore}}/S_{\text{Total}}$ = 0.4 and $V_{\text{Micropore}}/V_{\text{Total}}$ = 0.2), respectively. This is probably resulted from the significant shrinkage of the pore walls and the collapse of the mesostructure at high temperature.

Furthermore, with the increase of the pyrolysis temperature to 700 °C, the surface area due to micropores increased to 479 m^2 g^{-1}. These results may be due to the degradation of organic moieties in the framework during the formation of silica nanoparticles. The bridged organic moieties between silicon atoms (Si−CH_2−CH_2−Si) in the mesopore walls are cleaved to Si−CH_2CH_3 during pyrolysis process, and the carbonized films are produced with different carbon contents (relative to silica) under various pyrolysis temperatures, which will be shown later in the ^{29}Si and ^{13}C CP MAS NMR spectra in Figures 9, 10, and S3. With the increase of pyrolysis temperature to 900 °C, the carbonized carbon content decreased because of the formation of pyrolyzed gaseous molecules at high temperature. It is possible that the sequence of events (e.g., the cleavage to Si−CH_2CH_3 of Si−CH_2−CH_2−Si, the reduction of carbonized carbon contents, and the aggregation of silica nanoparticles at high temperature) led to the formation of defect spaces (e.g., micopores) in the mosopore walls. However, during the formation of the micropores, the film samples undergo significant shrinkage of the pore walls and a parial collapse of the mesostructure at high temperature. Therefore, with the increase of the pyrolysis temperature to 700 °C, although the pore volume due to micropores was between 0.20 cm^3 g^{-1} and 0.26 cm^3 g^{-1}, the total surface area and total pore volume decreased to 570 m^2 g^{-1} and to 0.31 cm^3 g^{-1}, respectively. On the other hand, at 900 °C, the surface area and pore volume due to the micropores decreased to 68.1 m^2 g^{-1} and 0.03 cm^3 g^{-1}, respectively. This may be due to the decrease in void spaces between silica nanoparticles because of the melting of the amorphous (noncrystallized) silica nanoparticles in the mesopore walls (the mesopore walls were composed of amorphous silica and crystallized silica (e.g., cristobalite), as shown in Table S1 in the Supporting Information) and a partial collapse of the mesostructure at high temperature of 900 °C. Accordingly, the total surface

(43) (a) Ashworth, J. R. *Phys. Chem. Miner.* **1988**, *15*, 246–251. (b) Withers, R. L.; Thompson, J. G.; Welberry, T. R. *Phys. Chem. Miner.* **1989**, *16*, 517–523. (c) Thompson, J. G.; Withers, R. L.; Palethorpe, S. R.; Melnitchenko, A. *J. Solid State Chem.* **1998**, *141*, 29–49.

Table 1. Structural Properties of the Samples Calculated Based on the N_2 Sorption

sample name	S_{Total} (m^2 g^{-1}) [a]	$S_{Micropore}$ (m^2 g^{-1}) [b]	V_{Total} (cm^3 g^{-1}) [c]	$V_{Micropore}$ (cm^3 g^{-1}) [d]	W (Å) [e]	D (Å) [f]
PMO film-EX	811	69.3	0.78	0.04	22.5	34.2
PMO film400	690	382	0.64	0.26	25.5	30.5
PMO film550	651	390	0.48	0.21	27.4	19.8
PMO film700	570	479	0.31	0.20	26.1	19.4
PMO film900	172	68.1	0.18	0.03	26.9	18.2

[a] Total surface area, BET method. [b] Micropore surface area, t-plot method. [c] Total pore volume. [d] Micropore volume, t-plot method. [e] Wall thickness, a_o − pore diameter (D), $a_o = d_{100}/\sqrt{3}$. [f] Pore diameter. The d_{100} was calculated by Bragg equation, $n\lambda = 2d\sin\theta$, where θ is an half of the degree of the (100) peak of the film.

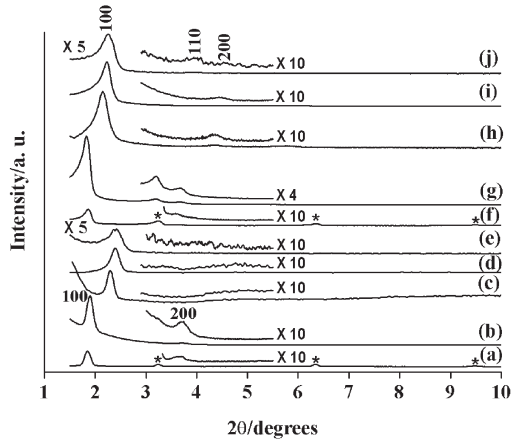

Figure 6. XRD patterns in the range of $2\theta = 1.5-10°$ of the (a−e) Na ion-containing, free-standing PMO films, (f−j) powdered PMO films, (a, f) as-synthesized PMO films, PMO films pyrolyzed at (b, g) 400, (c, h) 550, (d, i) 700, and (e, j) 900 °C in an Ar flow, respectively.

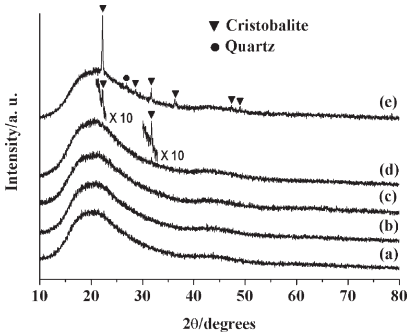

Figure 7. XRD patterns in the range of $2\theta = 10-80°$ of the (a) Na ion-containing, as-synthesized PMO film and PMO films pyrolyzed at (b) 400, (c) 550, (d) 700, and (e) 900 °C in an Ar flow, respectively.

area and total pore volume might decrease to 172 m^2 g^{-1} and to 0.18 cm^3 g^{-1}, respectively.

Figure 6 shows XRD patterns of the free-standing PMO films (Figure 6a−e) and powdered PMO films (Figure 6f−j) before (Figure 6a and f) and after pyrolysis (Figure 6b−e and g−j). The XRD patterns of the as-synthesized PMO films showed the 100 and 200 reflections (Figure 6a). This is consistent with the TEM observations (Figure 2a). The as-synthesized PMO film (Figure 6a) had a d_{100}-spacing of 46.5 Å. The star-signed diffraction peaks shown in Figure 6 were assigned to extra surfactant. These peaks disappeared after pyrolysis at 400 °C without cracking or loss of the mesostructure (Figures 6b, 2b and 2g). The absence of the 110 reflection for the films further confirmed that the long (c) axis of the mesostructure is oriented parallel to the surface. After pyrolysis at 400 °C (Figure 6b), the intensity of the diffraction peaks increased and the anticipated contraction (Δd_{100} = 1.2 Å) of the hexagonal *ab*-unit cell was observed. This was attributed to the removal of the surfactant template from the channels with the concomitant condensation of silanol (SiOH) groups on the pore walls.[31] After pyrolysis at 900 °C (Figure 6e), the mesostructure of the PMO films degenerated remarkably with a decreased *d*-spacing of 36.8 Å. However, the film still had an ordered mesostructure, which is consistent with the TEM observations (Figure 2e, j). Figure 6f shows an XRD pattern of the powdered sample obtained from the as-synthesized PMO film. The 100 and 200 diffraction peaks were observed along with other peaks (labeled by a star) due to extra surfactant. The 110 reflection was not observed due to overlap with the peak from the surfactant at 2θ = 3.2°. After pyrolysis at 400 °C (Figure 6g), the XRD pattern of the powdered PMO film showed the 100, 110, 200 reflections as expected, similar to data from previous reports.[31] After pyrolysis at 900 °C (Figure 6j), the intensity of the XRD pattern decreased remarkably. The above results suggest that an ordered mesostructure was maintained even though the mesostructure of the films collapsed remarkably with increasing pyrolysis temperature.

Figure 7 shows the XRD patterns of the PMO films before (Figure 7a) and after pyrolysis (Figure 7b−e) in the wide angle range. After pyrolysis at 700 and 900 °C (Figure 7d and e), the XRD patterns showed diffraction peaks due to the crystalline silica of cristobalites.[36b,37−39] This result corresponds to that from the HRTEM image in Figure 3. After pyrolysis at 900 °C, a trace amount of quartz was detected. At atmospheric pressure, quartz, tridymite and cristobalite are stable up to 870, 870−1470, and 1470−1700 °C, respectively. All phase transformations are kinetically inhibited and influenced by traces of impurities.[37] Indeed, the introduction of additives, such as alkali metal ions, plays an important role in producing a particular silica phase.[37,38] Venezia et al.[37] reported the effect of alkali ions on the amorphous to crystalline phase transition of silica between 500 and 1000 °C. In the present study, sodium hydroxide (NaOH) was used for the preparation of free-standing PMO films under basic conditions in reactant solutions. EDX revealed a Si/Na ratio of 9.5 in the as-synthesized PMO film. The production of crystalline silica cristobalite occurred during pyrolysis at temperatures above 700 °C. The C/Si ratio of the as-synthesized PMO film and the PMO film

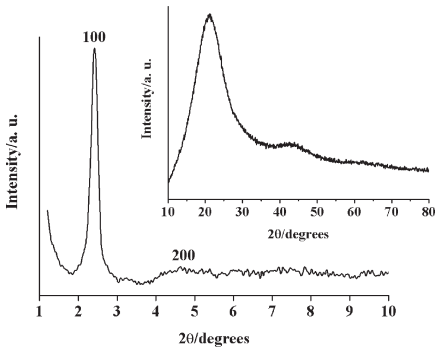

Figure 8. XRD pattern in the range of $2\theta = 1.2-10°$ of the free-standing, pyrolyzed PMO film at 900 °C for 3 h in an Ar flow without Na ions. The inset shows the XRD pattern in the range of $2\theta = 10-80°$.

pyrolyzed at 400, 550, 700, and 900 °C, respectively, were 1.9, 1.2, 1.1, 0.9, and 0.7. Without alkali metal ions, the XRD pattern (Figure 8) showed that crystalline silica could not form in the PMO film pyrolyzed at 900 °C in an Ar flow.

The ^{29}Si CP MAS NMR spectrum of the as-synthesized PMO film (Figure 9a) showed two signals at −61.2 and −69.3 ppm, which can be assigned to T^2 C(OH)*Si*$(OSi)_2$ and T^3 C*Si*$(OSi)_3$.[31,44] The ^{13}C CP MAS NMR spectra of the as-synthesized PMO films showed a peak at 6.3 ppm, which is assigned to carbon covalently linked to Si (Si−CH_2−CH_2−Si) (Figure 10a).[31,44] Peaks due to the surfactant carbon atoms were observed at 14.1, 23.2, 26.7, 30.5, 32.6, 53.7, and 67.0 ppm.[31] The NMR results confirmed that the organic−inorganic moiety (−Si−CH_2−CH_2−Si−) is the basic structural unit in the as-synthesized PMO film. After pyrolysis at 400 °C in Ar, the ^{29}Si CP MAS NMR spectrum (Figure 9b) showed two peaks (T^2 and T^3) between −40 and −78 ppm, demonstrating that the Si−C bonds were retained. The fraction of T^3 obtained from the fitted curves for the PMO film pyrolyzed at 400 °C in Ar (31.5% and 68.5% for T^2 and T^3, respectively) was higher than that of the as-synthesized PMO film (35.9% and 64.1% for T^2 and T^3, respectively), which is consistent with results of the XRD patterns (i.e., the decreasing *d*-spacing). The presence of Q-signals between −80 and −120 ppm suggests that the cleavage of some Si−C bonds occurred during pyrolysis. The Q/T ratio was 0.9. After pyrolysis at 550 °C in Ar (Figure 9c), the number of Q^n species (Q^3 and Q^4) increased, whereas the T^3 peak appeared at −63.6 ppm. The Q/T ratio was 2.3. Above 700 °C, the T-species of the ethylene-bridged silicon groups (−Si−CH_2−CH_2−Si−) disappeared and the Q-signal due to the siliceous matrix showed that Si−C bond cleavage occurred. When the film was pyrolyzed from 400 to 900 °C, various Q^n species from the Q-signals were observed via deconvolution by a curve-fitting calculation (Figure 9d,e). The estimated portions of Q^n species are tabulated in the Supporting Information (Table S1). It should be noted here that relative portions of Q^n species can be compared from

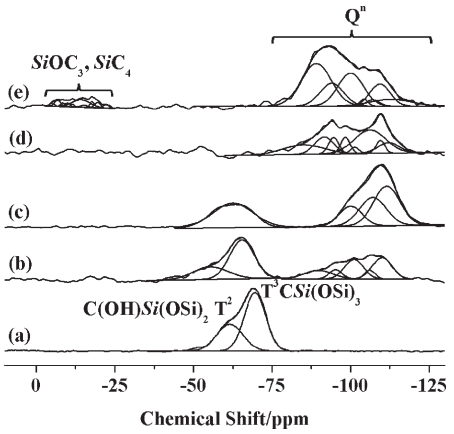

Figure 9. ^{29}Si CP MAS NMR spectra of (a) the Na ion-containing, as-synthesized PMO film and PMO films pyrolyzed at (b) 400, (c) 550, (d) 700, and (e) 900 °C in an Ar flow, respectively.

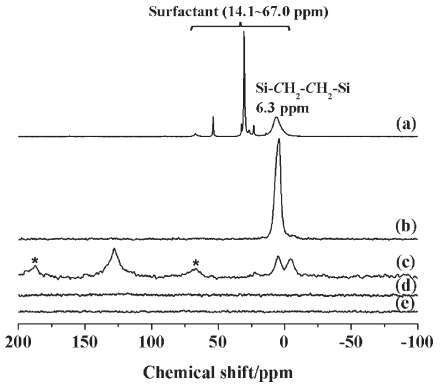

Figure 10. ^{13}C CP MAS NMR spectra in the range of $\delta = 200$ to −100 ppm of the (a) Na ion-containing, as-synthesized PMO film and PMO films pyrolyzed at (b) 400, (c) 550, (d) 700, and (e) 900 °C in an Ar flow, respectively. The asterisks (*) mark spinning side bands.

the tabulated values that were calculated from the area under the NMR spectra, though they may be not accurate values. The bonding geometry around the Si atoms and the nature of the species coordinated to the bridging oxygen (e.g., Si, H, Na, Al, etc.) also caused significant changes in the ^{29}Si chemical shifts.[45−53] The typical ranges were −81 to −88 ppm for Q^2, −89 to −102 ppm for Q^3, and −106 to −120 ppm for Q^4.[45−54] After pyrolysis at 400 °C (Figure 9b), five peaks for the Q-signal were

(44) (a) Inagaki, S.; Guan, S.; Fukushima, Y.; Ohsuna, T.; Terasaki, O. *J. Am. Chem. Soc.* **1999**, *121*, 9611–9614. (b) Melde, B. J.; Holland, B. T.; Blanford, C. F.; Stein, A. *Chem. Mater.* **1999**, *11*, 3302–3308.

(45) Charpentier, T.; Ispas, S.; Profeta, M.; Mauri, F.; Pickard, C. J. *J. Phys. Chem. B* **2004**, *108*, 4147–4161.
(46) Matijasic, A.; Lewis, A. R.; Marichal, C.; Delmotte, L.; Chézeau, J. M.; Patarin, J. *Phys. Chem. Chem. Phys.* **2000**, *2*, 2807–2813.
(47) Cho, H.; Felmy, A. R.; Craciun, R.; Keenum, J. P. *J. Am. Chem. Soc.* **2006**, *128*, 2324–2335.
(48) Mintova, S.; Petkov, N.; Karaghiosoff, K.; Bein, T. *Microporous Mesoporous Mater.* **2001**, *50*, 121–128.
(49) Ai, X.; Deng, F.; Dong, J.; Hu, W.; Xu, H.; Ye, C. *Solid State Nucl. Magn. Reson.* **2004**, *25*, 216–226.
(50) Mitra, A.; Kirby, C. W.; Wang, Z.; Huang, L.; Wang, H.; Huang; Yan, Y. *Microporous Mesoporous Mater.* **2002**, *54*, 175–186.
(51) Hamdan, H.; Muhid, M. N. M.; Endud, S.; Listiorini, E.; Ramli, Z. *J. Non-Cryst. Solids* **1997**, *211*, 126–131.
(52) Kümmerlen, J.; Merwin, L. H.; Sebald, A.; Keppler, H. *J. Phys. Chem.* **1992**, *96*, 6405–6410.
(53) Jones, A. R.; Winter, R.; Greaves, G. N.; Smith, I. H. *J. Phys. Chem. B* **2005**, *109*, 23154–23161.
(54) Sindorf, D. W.; Maciel, G. E. *J. Am. Chem. Soc.* **1983**, *105*, 1487–1493.

resolved at −89.8, −95.3, −101.1, −106.1, and −110.1 ppm. The silicon sites with resonances at −89.8, −95.3, and −101.1 ppm were attributed to Q^3 [$(SiO)_3Si(OH)$] or $(SiO)_3SiO^-Na^+$)] groups, while the silicon site with a resonance at −106.1 and −110.1 ppm was assigned to the Q^4 [$Si(OSi)_4$] group. In particular, the ^{29}Si chemical shift at −106.1 ppm was attributed to the silicon site in the Na ion-containing silica material.[55,56] After pyrolysis at 550 °C, three peaks from the Q-signal were resolved at −100.0 ppm for Q^3 and −106.5 and −111.5 ppm for Q^4, as shown in Figure 9c.

Our results showed that crystalline silica can be formed on the pores walls at a low pyrolysis temperature (e.g., above 700 °C) and under atmospheric pressure (e.g., Ar flow). After pyrolysis at 700 °C, the ^{29}Si CP MAS NMR spectrum of the sample consisted of eight peaks from the Q-signal (Figure 9d). In particular, the peak at −109.5 ppm indicated the presence of a crystalline silica phase. The amount of cristobalite in the PMO film 700 was estimated as 5.1% of Q^n species from the peak area analysis of the NMR spectra (see Table S1 in the Supporting Information),[45,51] which agrees with results from the XRD data. On the other hand, at pyrolysis temperatures of 700 and 900 °C, the existence of crystalline silica (cristobalite) was confirmed by the IR spectrum as well, with a characteristic cristobalite peak appearing at 623 cm^{-1} [45] (see Figure S4 in the Supporting Information).

After pyrolysis at 900 °C (Figure 9e), the Q^n species were resolved: −89.1, −94.1, −100.0, and −104.3 ppm for Q^3; and −107.1 −109.4, and −112.9 ppm for Q^4. The amount of cristobalite increased to 12.8% of the Q^n species (Table S1 in the Supporting Information). In addition, there was a small amount (2.3%) of quartz, as indicated by the small peak at −107.1 ppm (Table S1 in the Supporting Information).[45] The peaks around 112 ppm for Q^4 indicate the presence of an ill-ordered amorphous silica phase in a very highly dispersed form.[51] By increasing the pyrolysis temperature from 400 to 550 °C, the amount of Q^4 tetrahedral species increased from 41.1 to 79.9%, as shown in Table S1 in the Supporting Information. With a further increase in the pyrolysis temperature to 900 °C, the amount of Q^4 decreased to 23.1%, whereas the amount of Q^3 increased to 76.9%, probably because of the high level of silica consumption through carbothermal reduction between silica and carbon(Table S1 in the Supporting Information).[55] The Q^4 signal for tetrahedral species and the Q^3 and Q^2 for SiC or silicon oxide species were consumed. As shown in Figure 9e, a barely visible peak between −3.6 and −24.6 ppm was observed, suggesting an amorphous $SiOC_3$ or SiC_4 phase. The result is also supported by the XRD patterns, where no diffraction peaks for crystalline silicon carbide were observed (Figure 7e).[56−62] The broad peak can be deconvoluted with eleven peaks as shown in Figure 9e. The ^{29}Si chemical shifts from −5.0 to −8.5 ppm were assigned to $SiOC_3$ in the distorted structure or the different chemical environment with Na ion-containing silica/carbon composites in the framework, whereas the typical ^{29}Si chemical shift of $SiOC_3$ was approximately −5 ppm.[56−62] The signal from −9.9 to −23.5 ppm was assigned to amorphous SiC_4 species.[56−62] ^{13}C CP MAS NMR spectra provide information on the evolution of the local environment of the carbons during the pyrolysis process. The PMO film pyrolyzed at 400 °C showed an intense peak at 4.7 ppm, which was assigned to carbon linked covalently to Si (Si−CH_2−CH_2−Si) (Figure 10b).[31,44] At pyrolysis temperatures of 400 and 550 °C, the peaks from the surfactant at 14.1 to 67.0 ppm disappeared (Figure 10b, c). Broad peaks appeared at −6.1 and −4.6 ppm for PMO film400 (Figure S3(A-b)) and PMO film550 (Figure S3(A-c)), respectively. These peaks corresponded to the rearrangement products of Si−CH_2−CH_2−Si to Si−R, with R being a branched functional group. The change occurred simultaneously with the appearance of Q species. Ozin et al.[63] proposed a reaction mechanism between Si−C bonds and silanol groups converting a bridging methylene group into a terminal methyl group. Such a reaction mechanism can apparently be applicable to the bridging ethylene group, finally leading to the formation of a terminal ethyl group. We suggest the plausible mechanism of the cleavage of one Si−CH_2 bond to a bridging ethylene group, leading to ethyl groups terminally bonded to silicon during thermal treatment in argon. As suggested in the case of the methylene-bridged PMO, cleavage of one Si−CH_2 bond of bridging ethylene groups upon the addition of residual silanol groups or absorbed water in the sample may yield ethyl groups terminally bonded to the silicon (Scheme S1 in the Supporting Information.). The broad peaks at 128.0 ppm for PMO film550, 73.4, and 122.1 ppm for PMO film700 due to amorphous free-C were observed (Figure S3(B-c) and S3(B-d)), suggesting that the Si−C bonds were cleaved. The broad peaks at 122.1 and 128.0 ppm were assigned to amorphous sp^2-like carbon, whereas a broad peak at 73.4 ppm indicates the presence of sp^3-like carbon.[20a,b,58] After pyrolysis at 900 °C (Figure S3(B-e)), only a broad peak at 73.4 ppm for sp^3-like carbon was observed, indicating that all sp^2-like carbons were converted into sp^3-like carbon at high temperatures.

It should be noted that free-standing silica/carbon composite films have a cristobalite crystalline structure in the mesopore walls from ethylene-bridged organosilane, which can be distinguished from that of previous

(55) Wang, K.; Yao, J.; Wang, H.; Cheng, Y.-B. *Nanotechnology* **2008**, *19*, 175605–175612.
(56) Cao, F.; Li, X.-D.; Peng, P.; Feng, C.-X.; Wang, J.; Kim, D.-P. *J. Mater. Chem.* **2002**, *12*, 606–610.
(57) Hartman, J. S.; Richardson, M. F.; Sherriff, B. L.; Winsborrow, B. G. *J. Am. Chem. Soc.* **1987**, *109*, 6059–6069.
(58) Suyal, N.; Hoebbel, D.; Menning, M.; Schmidt, H. *J. Mater. Chem.* **1999**, *9*, 3061–3067.
(59) Liu, Q.; Shi, W.; Babonneau, F.; Interrante, L. V. *Chem. Mater.* **1997**, *9*, 2434–2411.
(60) Brus, J.; Kolár, F.; Machovic, V.; Svítilová, J. *J. Non-Cryst. Solids* **2001**, *289*, 62–74.
(61) Schiavon, M. A.; Redondo, S. U. A.; Pina, S. R. O.; Yoshida, I. V. P. *J. Non-Cryst. Solids* **2002**, *304*, 92–100.
(62) Czosnek, C.; Ratuszek, W.; Janik, J. F.; Olejniczak, Z. *Fuel Process. Technol.* **2002**, *79*, 199–206.
(63) Asefa, T.; MacLachlan, M. J.; Grondey, H.; Coombs, N.; Ozin, G. A. *Agew. Chem. Int. Ed.* **2000**, *39*, 1808–1811.

reports.[5,20a−20c] In addition, crystalline silicas were produced above 800 °C (In this work, crystalline silica species were formed above 700 °C in an Ar flow). It is quite different with the silica minerals that were formed at a high temperature and high pressure (~25 GPa).[39] Tsuchida and Yagi[40] reported a phase transformation from cristobalite and quartz to stishovite and another phase at high pressures (~60 GPa).

Our results showed that alkali metal ions were important in the formation of crystalline silica in the mesopore walls. Similar results (e.g., mesopore walls with crystalline silica species) were obtained with different alkali metal ions (Li, K, etc.) in the free-standing PMO films.

Finally, we carried out a hydrothermal stability test for 72 h in water at 100 °C with crystalline silica species and amorphous silica species containing mesoporous silica/carbon composite film. The test was carried out with the crushed film samples. The XRD data are provided in Figures S5 and S6 of the Supporting Information. Before and after hydrothermal treatment under the above condition, the crystalline silica-containing mesoporous silica/carbon composite film did not show noticeable changes in XRD patterns, meaning good hydrothermal stability. We also carried out the hydrothermal stability test for the amorphous silica-containing mesoporous silica/carbon composite film. The XRD data before and after hydrothermal treatment for the same conditions showed some thermal stability of the amorphous silica-containing mesoporous silica/carbon composite film as well. Careful inspection of Figures S5 and S6 in the Supporting Information, however, reveals that the XRD pattern of the amorphous silica-containing mesoporous silica/carbon composite film after hydrothermal treatment becomes slightly broader compared to that of the crystalline silica-containing mesoporous silica/carbon composite film, though all the samples showed three typical peaks (100), (110), and (200) with ordered 2D hexagonal symmetry before and after hydrothermal treatment. The results suggest that the hydrothermal stability of the crystalline silica-containing mesoporous silica/carbon composite film is slightly improved when compared to that of amorphous silica-containing mesoporous silica/carbon composite film.

Before concluding, it should be noted that fabrication of the desired morphologies as well as control of the composition, structure, porosity, etc. are important for a variety of practical applications of mesoporous materials. In particular, mesoporous films can be applied in many diverse fields, especially in opto-electronic thin-film devices such as organic light-emitting devices (OLED), solar cells, photocatalysis, etc. To apply the mesoporous materials to opto-electronic devices or effective photocatalysis, they must be in the form of film. Such applications can be found in the literature. For example, Shioya et al. reported that transparent Ti-containing mesoporous silica thin film materials exhibited unique photocatalytic activity for the reduction of CO_2 with H_2O.[64] Furthermore, in our laboratory, we applied mesoporous thin films in organic light emitting devices.[65] Solar cells using mesoporous thin films were reported by Lancelle-Beltran et al.,[66a] Zhukalova et al.,[66b] and Crossland et al.[66c] These reports all showed an improvement in device performance when using mesoporous thin films in comparison to conventional thin film devices without mesoporous films.

Conclusions

The incorporation of organic functional groups into the pore walls not only results in interesting ordered mesoporous organosilica structures but can also provide a precursor for the fabrication of nanocomposite materials with improved thermal, chemical, and mechanical properties. Free-standing mesoporous silica/carbon composite films were successfully synthesized from an ethylene-bridged organosilica/surfactant mesophase via a pyrolysis process. After pyrolysis from 400 to 900 °C, the film thickness was reduced from 356 to 192 nm with a uniform size. The nanocomposite films had a highly ordered periodic mesostructure with a hexagonal closed-packed arrangement of channels running parallel to the film surface. Amorphous silica walls were formed in the mesopore walls of the PMO film pyrolyzed at 900 °C in Ar without alkali metal ions. On the other hand, the films pyrolyzed above 700 °C in the presence of alkali metal ions had a cristobalite crystalline silica wall structure. The ordered mesostructure was retained up to 900 °C. At pyrolysis temperatures between 400 and 900 °C, the pore diameter, surface area, and pore volume of the free-standing mesoporous silica/carbon composite films obtained from N_2 sorption isotherms were determined to be 18.2−30.5 Å, 172−690 $m^2\ g^{-1}$, and 0.18−0.64 $cm^3\ g^{-1}$, respectively.

Acknowledgment. This work was supported by the Korea Foundation for International Cooperation of Science and Technology (KICOS, now merged to the National Research Foundation of Korea(NRF)) through the Korea-China Joint Research Center Program on Mesoporous Thin Films (K20807000001-09B1200-00110), the NRF through Acceleration Research Program (2009-0078791), and the Brain Korea 21 Project funded by Ministry of Education, Science and Technology, Korea.

Supporting Information Available: TGA curve of the as-synthesized PMO film recorded under nitrogen atmosphere, photographs of the as-synthesized and the carbonized free-standing PMO film at 900 °C for 3 h in an Ar flow, IR and

(64) Shioya, Y.; Ikeue, K.; Ogawa, M.; Anpoa, M. *Appl. Catal. A: General* **2003**, *254*, 251–259.

(65) Park, J.-W.; Park, S. S.; Kim, Y.; Kim, I.; Ha, C.-S. *ACS Nano* **2008**, *2*(6), 1137–1142.

(66) (a) Lancelle-Beltran, E.; Prené, P.; Boscher, C.; Belleville, P.; Buvat, P.; Lambert, S.; Guillet, F.; Boissiére, C.; Grosso, D.; Sanchez, C. *Chem. Mater.* **2006**, *18*, 6152–6156. (b) Zukalová, M.; Zukal, A.; Kavan, L.; Nazeeruddin, M. K.; Liska, P.; Gra1tzel, M. *Nano Lett.* **2005**, *5*, 1789–1792. (c) Crossland, E. J. W.; Kamperman, M.; Nedelcu, M.; Ducati, C.; Wiesner, U.; Smilgies, D.-M.; Toombes, G. E. S.; Hillmyer, M. A.; Ludwigs, S.; Steiner, U.; Snaith, H. J. *Nano Lett.* **2009**, *9*(8), 2807–2812.

^{13}C CP MAS NMR spectra in the range of $\delta = 0$ to -30 ppm and $\delta = 145-50$ ppm of the Na ion-containing, as-synthesized PMO film and PMO films pyrolyzed at various temperatures in an Ar flow, schematic representation of the cleavage of one $Si-CH_2$ bond to a bridging ethylene group leading to ethyl groups terminally bonded to silicon, XRD patterns in the range of $2\theta = 1.5-10°$ and $2\theta = 10-80°$ of the crushed and the hydrothermal treated at 100 °C for 72 h mesoporous silica/carbon composite film with amorphous silica species and crystalline silica species after pyrolysis at 900 °C in an Ar flow, and tabulated data of the chemical shift and portions of Q^n species obtained from PMO films pyrolyzed at different temperatures (PDF). This material is available free of charge via the Internet at http://pubs.acs.org.